Research Paper

Cu₂O nanocrystals/TiO₂ microspheres film on a rotating disk containing long-afterglow phosphor for enhanced round-the-clock photocatalysis

Ying Lu[a], Xu Zhang[a], Yicong Chu[a], Hongbin Yu[a], Mingxin Huo[a,b], Jiao Qu[a], John C. Crittenden[c,d], Hongliang Huo[a,*], Xing Yuan[a,*]

[a] School of Environment, Northeast Normal University, Changchun, 130024, China
[b] State Environmental Protection Key Laboratory of Wetland Ecology and Vegetation Restoration, Changchun, 130117, China
[c] Brook Byers Institute for Sustainable Systems, Georgia Institute of Technology, Atlanta, GA 30332, United States
[d] School of Civil & Environmental Engineering, Georgia Institute of Technology, Atlanta, GA 30332, United States

ABSTRACT

A Cu₂O nanocrystals/TiO₂ microspheres (Cu₂O NCs/M-TiO₂) rotating disk reactor assisted by long-afterglow phosphor was successfully designed and fabricated in order to achieve enhanced round-the-clock photocatalysis. The Cu₂O NCs/M-TiO₂ composite exhibited good photocatalytic activity owing to enlarged light absorption and efficient quantum yield by integrating Cu₂O NCs with core-shell M-TiO₂. Through rotating the catalyst disk, a thin aqueous film was formed on its upper part as well as continuously refreshed. Compared with bulk reaction, the photon propagation distance within this film was greatly shortened, and the possibility of light absorption by solution was correspondingly reduced, increasing the light utilization yield of photocatalytic system. Additionally, the continuous update of pollutants and their intermediates on catalyst was beneficial to photocatalysis. The long-afterglow phosphor in reactor could absorb excessive light energy and give out persistent fluorescence, exciting Cu₂O NCs/M-TiO₂ composite and realizing round-the-clock photocatalysis. As a result, the Cu₂O NCs/M-TiO₂ rotating disk reactor containing long-afterglow phosphor presented high reactivity in the photocatalytic degradation of rhodamine B and bisphenol A. The recycle experiments confirmed the stability and reliability of prepared reactor.

1. Introduction

Photocatalytic oxidation has attracted much attention in recent years because of the employ of stable, non-toxic photocatalysts, direct utilization of solar light and complete contaminants degradation. Until now, this technique has been applied to various actual wastewater treatment systems, such as textile wastewater [1,2], papermaking wastewater [3,4], petroleum refinery wastewater [5], hospital wastewater [6] and so on. However, there are three main problems preventing the full industrialization of photocatalysis. One is that photocatalytic process cannot proceed at night because of the absence of light source which could excite semiconductor. It is crucial to realize the round-the-clock photocatalysis, for instance by transforming the redundant energy during light illumination to a mediate which could continuously supply energy in dark [7,8]. Another limiting factor is the low light utilization yield on account of light-shielding effect by solution, especially by the colorful liquid; accordingly, the photocatalyst could not be sufficiently activated by sunlight, leading to less

photoelectron/hole pair generation and the consequent low treatment efficiency [9–11]. The third problem is the poor performance of photocatalyst. Although TiO₂ has been widely analyzed owing to cheapness, nontoxicity and stability, its practical application is still restricted due to narrow light response region and low quantum efficiency [12,13].

The photodegradation of pollutants involves semiconductor excitation by light, photoelectron/hole pair generation and migration, oxidizing and reductive species formation and the subsequent contaminants decomposition. Among these steps, the light activation is essential, since it directly determines the quantity of photoinduced carriers which are responsible for pollutants degradation. If the light irradiation is ceased, at night, for example, the catalytic reaction will be also stopped, reducing the photocatalytic efficiency and limiting the widespread applications of photocatalytic technology. A fascinating strategy for round-the-clock contaminates treatment should be established. Recently, some efforts have been paid to combine semiconductor with long afterglow phosphors, which could be excited by

irradiated light and thus emit long lasting phosphorescence after the removal of light source, activating semiconductor and achieving persistent photocatalysis [14,15]. Previous works have demonstrated that these "catalytic memory" composite which maintained photocatalytic activity in dark possessed distinguished catalytic capability in the decomposition of acetaldehyde, rhodamine B, methyl orange, etc [16,17]. Among these materials, the aluminate phosphors have been widely applied for photocatalysis because of outstanding stability in aqueous solution for a long time [15,17].

It is known from the photocatalytic procedure that light has to penetrate the contaminants solution prior to reaching the catalysts surface, resulting in virtual light energy loss and the consequently depressed pollutant degradation. On the basis of Beer's law [18],

$$A = \varepsilon bc \tag{1}$$

where A is the absorbance; b is the path length; and c is the solution molarity. The photon loss owing to liquid absorption could be decreased by shortening its propagation path length. Therefore, a new rotating disk reactor has been proposed by Dionysiou's group [19,20]. Unlike traditional immobilized reactor, this catalyst disk keeps rotating, through which a micrometer-scale aqueous film is coated on the upper part, whereas the lower part is immersed in wastewater and performs conventional bulk-phase treatment. Within this thin liquid film, the light energy loss through absorption by contaminants solution dramatically reduced, increasing the light utilization yield of photocatalytic system [21]. Furthermore, the mass transfer on photocatalyst and dissolved oxygen content in solution could be extremely enhanced by this persistent rotation.

In order to achieve catalyst with high photocatalytic activity, many endeavors have been devoted. The first kind of approaches is to improve the performance of pristine TiO_2 by metal ion doping [22], nonmetal doping [23], dye sensitization [24], and so forth. The other way is to develop new photocatalyst, sulfides [25], complex oxides [26], and plasmonic catalysts [27], for example. Sensitization of TiO_2 with narrow band gap semiconductor could utilize the excitation of narrow band gap catalyst to extend the working range of TiO_2 and the heterojunction between these two materials to suppress the photocarriers recombination, displaying high photocatalytic capability [28]. Cu_2O with the band gap of 2.17 eV is considered as an attractive material for its great potential application in solar conversion, catalysis, and sensing [29]. The Cu_2O/TiO_2 composite has presented excellent photocatalytic performance under visible-light illumination [30–32]. Besides chemical ways, physical approaches through structural or morphological modifications also greatly affect the catalyst light harvest, reactant molecules adsorption, and photoelectron/hole pair migration. The core-shell microspheres structure is favorable for pollutant degradation, which could be attributed to the enhanced light harvest resulted from the multiple reflections and scattering of light within the core-shell structure [33,34].

As stated above, a Cu_2O nanocrystals/TiO_2 microspheres (Cu_2O NCs/M-TiO_2) rotating disk reactor assisted with long-afterglow phosphor was designed and synthesized for enhanced round-the-clock photocatalysis. This novel photocatalytic reactor could achieve (1) persistent photocatalysis owing to the assistance of long afterglow phosphor, breaking through the sunlight irradiation limitation of photocatalytic technology; (2) increased light utilization yield of photocatalytic system via keeping the catalyst disk rotating, which also benefited the update of pollutants and intermediates on catalyst; (3) high photocatalyst reactivity thanks to the enlarged optical response region and improved quantum efficiency by integrating Cu_2O nanocrystals with TiO_2 microspheres. To the best of our knowledge, this is the first investigation of combining persistent excitation, increased system light utilization and high catalyst activity for enhanced round-the-clock photocatalysis. Rhodamine B (RhB) and bisphenol A (BPA) were employed as model contaminates to evaluate the photocatalytic capability of proposed catalytic system.

2. Experimental

2.1. Catalysts preparation

Fabrication of M-TiO_2. The synthesis method of core-shell TiO_2 microspheres (M-TiO_2) has been reported by Guo et al. [33]. Certain amount $TiCl_4$, $(NH_4)_2SO_4$, and $CO(NH_2)_2$ were respectively dissolved in deionized water under ice-water bath. After stirring for 4 h, CH_3CH_2OH was slowly dropped into above mixture and formed a transparent solution, in which the molar composition of $TiCl_4$: H_2O: CH_3CH_2OH: $(NH_4)_2SO_4$: $CO(NH_2)_2$ was 1: 73: 23: 1: 18. Then, the mixture was transferred into a Teflon-lined autoclave and maintained at 368 K for 24 h. After cooling to room temperature, the precipitate was filtered and washed with ethanol and deionized water, and further calcined at 733 K for 2 h with a heating rate of 2 K/min.

Fabrication of Cu_2O NCs/M-TiO_2. The Cu_2O nanocrystals (Cu_2O NCs) were integrated with M-TiO_2 via a hydrothermal reduction method reported by our group [31]. The M-TiO_2 was first dispersed into $Cu(CH_3COO)_2$ solution and then immersed into NaOH aqueous solution. After washing with deionized water and drying in air, the sample and 0.5 mM glucose solution (30 ml) were transferred into an autoclave with the volume of 50 ml and kept at 369 K for 10 h. The M-TiO_2 incorporated with Cu_2O NCs was named as X-Cu_2O NCs/M-TiO_2, where X represented the impregnation times in $Cu(CH_3COO)_2$ and NaOH solution.

Fabrication of Cu_2O NCs/M-TiO_2 rotating disk. Under dark, ventilated, and clean conditions, the UV glue was smeared onto quartz sheet, which has already been sonicated in hydrochloric acid, acetone and deionized water, respectively, in order to remove the surface impurities. Then, the Cu_2O NCs/M-TiO_2 photocatalyst was evenly dispersed on the UV glue and then irradiated under UV lamp for 10 min, obtaining Cu_2O NCs/M-TiO_2 catalyst film. Finally, four sheets coated with Cu_2O NCs/M-TiO_2 film were attached on a quartz disk (7.5 cm diameter), whose chambers have already been filled with long-afterglow phosphor (Foshan Xiuqing Chemical Co., Ltd). $SrAl_2O_4$: (Eu, Dy) is an excellent long afterglow phosphor emitting yellow green light, showing the possibility to excite prepared composite photocatalyst.

2.2. Characterization

A Micro FEI PHILIPS XL-30-ESEMFEG field emission scanning electronic microscope (SEM) operated at 20 kV was used to obtain the scanning electron microscopy images and corresponding energy dispersive X-ray spectroscopy (EDS). A Hitachi Su 8020 microscope with an X-ray energy dispersive spectrometer was utilized to get the SEM-EDS mapping. A EM-2100F high resolution transmission electron microscope (TEM) was employed to get the transmission electron microscope and high resolution transmission electron microscope (HRTEM) images. A Rigaku D/max-3c X-ray diffractometer (XRD) with Cu Kα radiation was exploited to gain the X-ray diffractometer (XRD) pattern. A VG-ADES 400 instrument with Mg kα as the excitation source was utilized to achieve the X-ray photoelectron spectroscopy (XPS) data. A Shimadzu UV-2450 UV–vis spectrophotometer, which used $BaSO_4$ as reflectance standard, was utilized to get the absorption spectra. A Varian Cary Eclipse Spectrometer fluorescence spectrometer was employed to obtain the photoluminescence (PL) spectra. A Bruker ER073 spectrometer was used to detect the signals of hydroxyl radicals and superoxide radicals.

2.3. Photocatalytic test

The degradation of RhB and BPA were carried out respectively in prepared rotating disk reactor assisted by long-afterglow phosphor, as illustrated in Fig. S1. All the experiments were conducted at room temperature. Prior to illumination, the quartz disk coated with Cu_2O NCs/M-TiO_2 composite was rotated for 30 min in dark at a certain

speed until reaching the adsorption-desorption equilibrium. Then, the photocatalytic reaction was initiated by illumination with a 300 W xenon lamp (PLS-SXE300, Beijing Trusttech, China) at a distance of 30 cm away. All the UV light with wavelength less than 420 nm was cut off by glass filters (JB-420). Each reaction lasted for 3 h, and certain amount pollutant solution was collected at 30 min intervals for analysis. The RhB concentration change was monitored by a UV–vis spectrophotometer (Shimadzu double-beam spectrophotometer UV-190) at the characteristic wavelength of 553 nm, while the concentration variation of BPA was measured on a Shimadzu LC-20A high pressure liquid chromatography (HPLC) using methanol and water (75/25, v/v) as the mobile phase.

2.4. Photoelectrochemical measurements

The photocurrent (PC) responses and electrochemical impedance spectroscopy (EIS) measurements were carried out on a CHI 660 B electrochemical workstation (Shanghai, China) in a standard three electrode model, utilizing a Pt foil as the counter electrode and an Ag/AgCl electrode as the reference electrode. Na_2SO_4 (0.1 M) was used as the electrolyte solution without any additive. The working electrode was prepared as follows: 10 mg as-prepared catalyst was ultrasonicated in 2 ml ethanol to disperse it evenly and get slurry which was then spin-coated on a Ti plate (2.1×2.1 cm^2). After air drying, the working electrode was further dried at 333 K for 24 h to improve adhesion. The light source was the same as that used in photocatalysis. The EIS was performed at the open-circuit potential with the frequency ranged from 0 to 100 kHz.

3. Results and discussion

3.1. Morphology

The morphologies of pristine M-TiO$_2$ and 2-Cu$_2$O NCs/M-TiO$_2$ were characterized by SEM and TEM, respectively. As presented in Fig. 1a, the diameter of TiO$_2$ microspheres was in the range of 1.5–4 μm. High magnification SEM image displayed in Fig. 1b illuminated that the TiO$_2$ microsphere was comprised of connected crystalline with the size of 10–20 nm. No Cu$_2$O NCs was seen in the SEM images of 2-Cu$_2$O NCs/M-TiO$_2$, which could be attributed to its small particle size, high distribution, and similar semiconductor properties with TiO$_2$. But the energy dispersive X-ray spectroscopy (EDS) analysis demonstrated the existence of elements Ti, O, Cu, respectively, as presented in Fig. 1f. Furthermore, the elemental distribution of 2-Cu$_2$O NCs/M-TiO$_2$ was characterized by SEM-EDS mapping. As shown in Fig. S2, the green, red, and yellow colors represented the elements Ti, O, and Cu, respectively. This result confirmed that element Cu was well distributed on the surface of TiO$_2$ microsphere, in agreement with the proposed morphology of Cu$_2$O/TiO$_2$ composition. From the TEM image of 2-Cu$_2$O NCs/M-TiO$_2$ shown in Fig. 1g, the TiO$_2$ microsphere exhibited a distinctive core-shell structure. The diameter of the core was around 500–600 nm, and the shell thickness was about 20–30 nm. Cu$_2$O NCs whose average size was approximately 10 nm were conformably distributed on the surface of M-TiO$_2$. In Fig. 1h, the lattice spacing of 0.24 nm matched with the (111) plane of Cu$_2$O, and the lattice space of 0.35 nm corresponded to the (101) crystal plane of anatase TiO$_2$. This result confirmed the successful integration of Cu$_2$O NCs with M-TiO$_2$, which was beneficial to efficient light harvesting owing to the visible light response of Cu$_2$O NC and high quantum yield because of the heterojunctions between Cu$_2$O and TiO$_2$.

3.2. XRD and XPS analysis

Fig. S3 shows the XRD patterns of pure M-TiO$_2$, 1-Cu$_2$O NCs/M-TiO$_2$, 2-Cu$_2$O NCs/M-TiO$_2$, and 3-Cu$_2$O NCs/M-TiO$_2$. The diffractive peaks at 25.3°, 37.9°, 48.1°, 53.9°, 55.1°, and 63.1° were respectively

corresponded to the (101), (004), (200), (105), (211), and (204) crystal plane of anatase TiO$_2$ (JCPDS 21–1272). No significant diffraction peak of Cu$_2$O was observed although its deposition times have reached three, which could be mainly ascribed to the low content incorporation. The XPS spectra were further conducted. As presented in Fig. 2b, the Ti species were displayed in Ti^{4+} phase, corresponding to the binding energies of 458.2 and 464.0 eV in Ti $2p_{3/2}$ and Ti $2p_{1/2}$ levels, respectively, while the shoulder peak was ascribed to the Ti^{4+} state in Ti-O-Cu structure, which was beneficial to the charge transfer between TiO$_2$ and Cu$_2$O [35,36]. The peaks located at 932.0, 952.2, and 955.1 eV were known as the characteristic of Cu$^+$ in Cu$_2$O NCs, and the satellite peak was attributed to the shakeup of outer electron in Cu(I) [31,37,38]. The peak at the binding energy of 529.5 eV was credited to Ti-O and Cu-O species, whereas the one at 531.2 eV was assigned to the O−H bond of hydroxyl group or water molecules adsorbed on catalyst surface [37,39]. These results clearly proved the presence of TiO$_2$ and Cu$_2$O, in concert with the characterization of SEM and TEM.

3.3. Optical properties

The light absorption properties of prepared catalysts were measured by using a UV–vis diffuse reflectance spectrometer. From Fig. 3a, the absorption edge of pure M-TiO$_2$ occurred at about 380 nm, which was on account of its large band gap energy. The integration of Cu$_2$O NCs expanded the optical response range of M-TiO$_2$ to visible light region, which benefited from the visible-light-driven behavior. However, as the Cu$_2$O content consistently increased, the Cu$_2$O NCs became larger and packed in a much compact way, resulting in the enhancement of light reflection and the consequent reduction of light absorption [21,40,41]. In the absorption spectra, 2-Cu$_2$O NCs/M-TiO$_2$ exhibited the highest light harvesting. The result was thanks to the cooperated light absorption of TiO$_2$ and Cu$_2$O. Additionally, the multiple reflections and scattering of light within the core-shell structure of M-TiO$_2$ was favorable to reinforce the interaction between photons and catalyst, enhancing the light absorption of 2-Cu$_2$O NCs/M-TiO$_2$. Inset of Fig. 3a was the corresponding Tauc plots for the bandgap estimation of prepared samples [42]. The extrapolation of the linear region to photon energy axis yielded the bandgap values as 3.12 eV for M-Ti$_2$O, 2.91 eV for 1-Cu$_2$O NCs/M-TiO$_2$, 2.87 eV for 2-Cu$_2$O NCs/M-TiO$_2$, and 2.88 eV for 3-Cu$_2$O NCs/M-TiO$_2$, consistent with their optical properties. From the PL spectrum presented in Fig. 3b, the long-afterglow phosphor emitted visible light with broad spectrum from ca. 430 nm to ca. 520 nm, showing an overlapping with the absorption spectra of as-prepared photocatalysts. This matching suggested the opportunity of long-afterglow phosphor as a light source to excite Cu$_2$O NCs/M-TiO$_2$ composite.

3.4. PL spectra

To further investigate the optical quality of prepared catalysts, PL spectra were depicted in Fig. 4. The excitation wavelength was determined as 320 nm. Pure TiO$_2$ presented strong luminescence in a broad range (350–420 nm), confirming the generation of photoinduced electron/hole pair and the next recombination process. For Cu$_2$O NCs/M-TiO$_2$, the PL intensities decreased obviously, indicating the photocarriers recombination was effectively inhibited by the *p-n* heterojunction between TiO$_2$ and Cu$_2$O [31]. With the increase of Cu$_2$O NCs loading amount, the PL peak intensity reduced, implying the electron/hole recombination rate decreased due to the enhanced number of heterojunctions. However, as the Cu$_2$O NCs content continue increase, the PL peak intensity became stronger, owing to the fact that excessive Cu$_2$O NCs could provide recombination center for photocarriers. Finally, 2-Cu$_2$O NCs/M-TiO$_2$ displayed the lowest peak intensity among all the materials and thus was wished to present high photocatalytic activity.
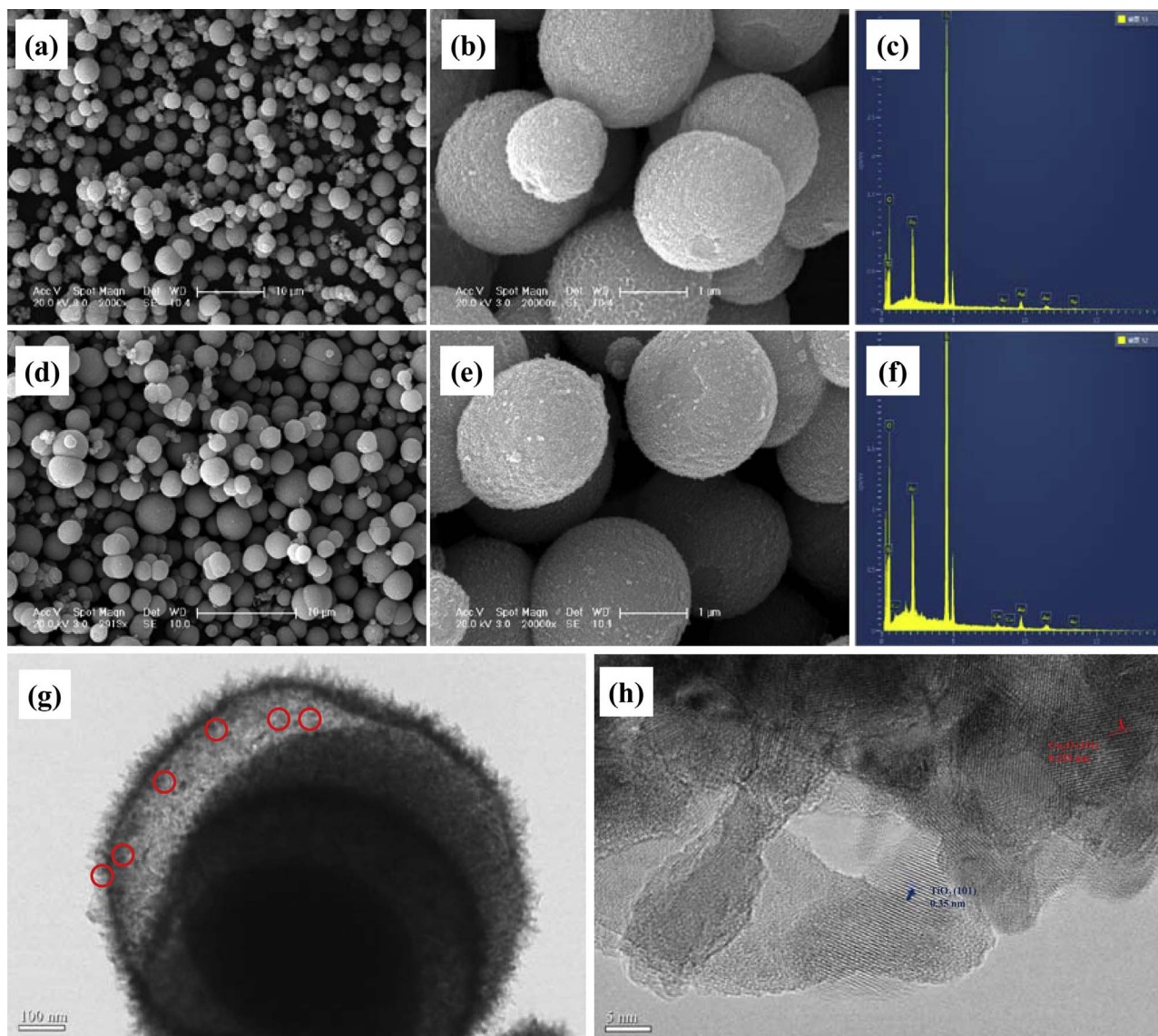
Fig. 1. SEM images and EDS of M-TiO$_2$ (a–c) and 2-Cu$_2$O NCs/M-TiO$_2$ (d–f), and TEM (g) and HRTEM (h) images of 2-Cu$_2$O NCs/M-TiO$_2$.

3.5. Photoelectrochemical performance

In terms of photocatalytic process, the efficient separation and transport of photoinduced carriers is also significant. The PC responses of prepared photocatalysts were conducted and shown in Fig. 5a. It can be seen that all the samples exhibited good photocurrent reproducibility when the light was switched on and off. Compared to bare M-TiO$_2$, the Cu$_2$O NCs/M-TiO$_2$ composite presented enhanced photocurrent densities, certifying that the electron/hole pairs recombination was efficiently suppressed by the integration of Cu$_2$O with TiO$_2$. With the increase of Cu$_2$O NCs amount, the photocurrent increased first and thereafter decreased, which could be attributed to the increased scattering effect of photons and recombination centers of carriers through excess Cu$_2$O NCs in the photosystem [40,41]. The photocurrent density of 2-Cu$_2$O NCs/M-TiO$_2$ was much higher than those of other catalysts, revealing the more efficient generation and prolonged lifetime of photogenerated charge carriers, which was critical to excellent photocatalytic activity. To gain deeply insight into the effect of Cu$_2$O NCs on the charge transport behaviors of Cu$_2$O NCs/M-TiO$_2$ composite, the EIS was investigated. It is well-established that the arc radius in EIS Nyquist plot could reflect the reaction rate on the surface of electrode. Normally, a smaller radius corresponds to a lower electron-transfer

resistance and thus implies a high efficiency of charge transfer and separation [43,44]. In the EIS spectra (Fig. 5b), all the electrodes presented similar semicircular Nyquist plots, among which the arc radius of 2-Cu$_2$O NCs/M-TiO$_2$ was the smallest, suggesting a higher separation efficiency of photoinduced electron/hole pairs and a faster interfacial charge transfer, which was in good accordance with the results of PC measurements.

3.6. Photocatalytic removal of RhB

Batch experiments were performed to investigate the parameters affecting the photocatalysis of Cu$_2$O NCs/M-TiO$_2$ rotating disk reactor assisted by long-afterglow phosphor, such as the loading amount of Cu$_2$O in hybrid photocatalyst, catalyst dosage, rotating speed, catalyst type and so on.

3.6.1. Effect of Cu$_2$O loading amount

The loading amount of Cu$_2$O NCs is a significant factor that affects the photocatalytic performance of Cu$_2$O NCs/M-TiO$_2$ composite. As presented in Fig. S4, the pristine M-TiO$_2$ displayed poor photocatalytic activity because of its wide band gap. After the incorporation of Cu$_2$O NCs, RhB degradation percentage increased due to the enlarged light
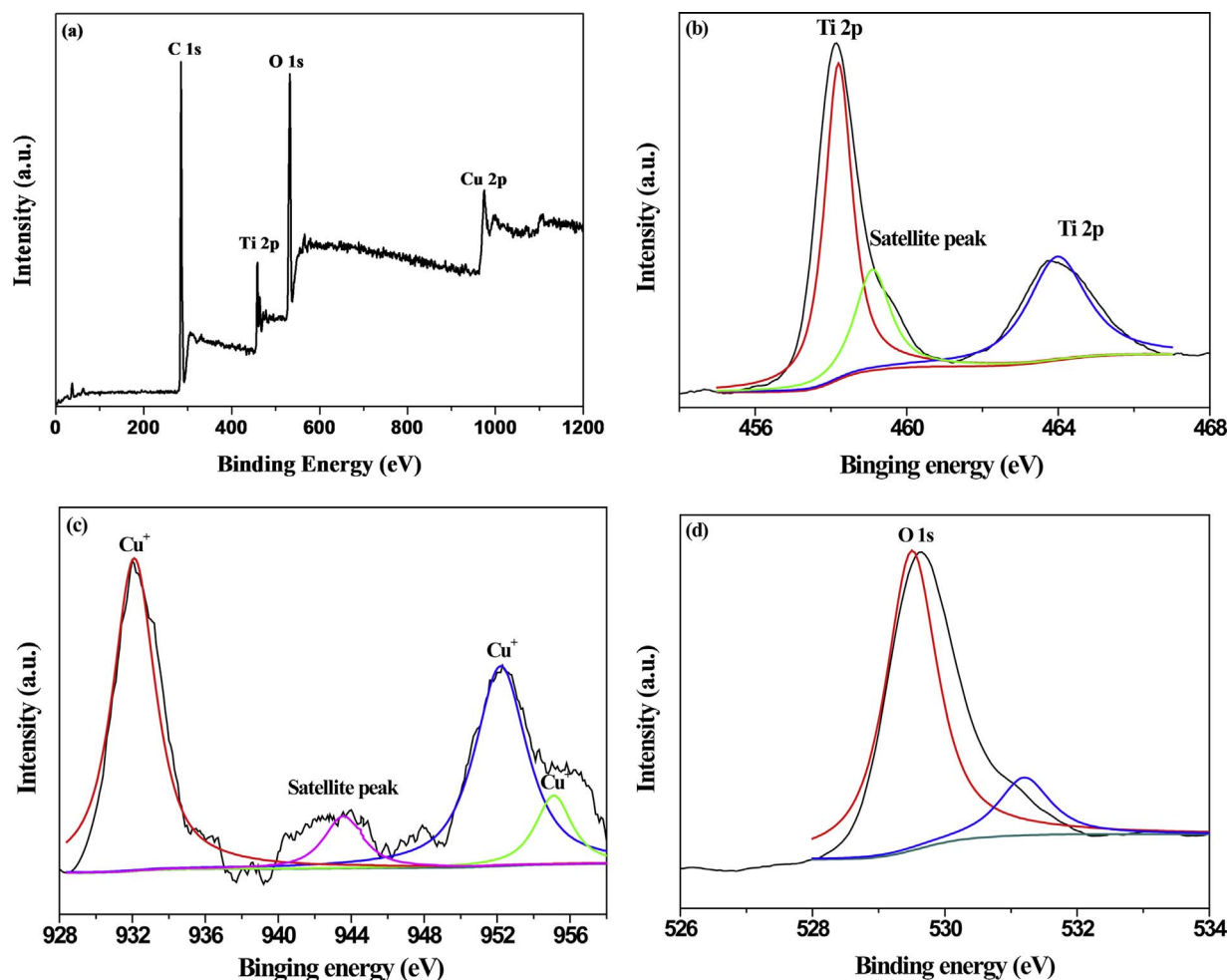
Fig. 2. XPS spectra of 2-Cu$_2$O NCs/M-TiO$_2$: full spectrum (a), Ti spectrum (b), Cu spectrum (c), and O spectrum (d).

response range and efficient charge transfer. But too high Cu$_2$O content was harmful for contaminate decomposition, which was resulted from the reduced light absorption and decreased quantum yield. Finally, 2-Cu$_2$O NCs/M-TiO$_2$ was determined as the optimum catalyst, which decomposed more than 77% RhB after 3 h irradiation. This result could be attributed to the enhanced light harvesting by integrating Cu$_2$O NCs with core-shell TiO$_2$ microspheres and suppressed photocarriers recombination owing to the heterojunction between *p*-type Cu$_2$O and *n*-type TiO$_2$.

3.6.2. Effect of catalyst dosage

The effect of changing catalyst dosage on RhB degradation was investigated and shown in Fig. S5. With the increase of catalyst dosage, pollutant degradation rate in this rotating disk reactor increased. This enhancement was attributed to the improved production of photo-generated electrons, holes, and other reactive oxygen species responsible for RhB removal. However, as the catalyst dosages continually increased, extremely crowded and even the overlap of Cu$_2$O NCs/M-TiO$_2$ composite catalysts were deposited on the quartz glass, which went against the effective utilization of catalyst. At the same time, taking into account the increase in catalyst thickness would reduce the degree of adhesion between catalyst and quartz sheet, the optimum catalyst loading was 0.4 g.

3.6.3. Effect of rotating speed

Rotation speed is one of the most important operation parameter affecting the photocatalytic process, for which is related to the thickness of carried liquid film as well as the mass transfer coefficients of

contaminates, intermediates and molecule oxygen. The thickness of aqueous film on rotating disk can be calculated according to following equation [45,46],

$$\delta = 1.2(V_c)^{0.5}(10^{-4}m) = 1.2(Rw)^{0.5}(10^{-4}m) \tag{2}$$

where δ is the average film thickness, *Vc* is the vertical component of the peripheral velocity at the point where the disk emerges from the water, *R* is the distance between the disk center to the studied point, and ω is the angular velocity. From this formula, it can be found that the aqueous film thickness increases when the speed is faster.

The influence of rotating speed on RhB decomposition was investigated, as presented in Fig. 6. As the rotating speed increased from 30 to 120 rpm, the pollutant degradation rate first increased and then decreased. The highest photocatalytic performance achieved when the rotation speed was 90 rpm. Within a certain rotation speed range, the RhB removal rate increased with increasing the aqueous film thickness because more pollutant molecules could be provided to photocatalyst and eventually be degraded. Meanwhile, the update of RhB and oxygen on catalyst surface were strengthened, finally exhibiting improved photocatalytic capability. While as the rotation speed was high enough, the decomposition efficiency declined, which was resulted from the fact that too thick liquid film was unfavorable to the interaction among catalyst, RhB, and dissolved oxygen.

3.6.4. Effect of catalyst type

The photocatalytic reactivity of other catalyst, such as Cu$_2$O NCs, P25, M-TiO$_2$, 2-Cu$_2$O NCs/P25 were also studied. First-order kinetics were observed and presented in Fig. 7. The corresponding kinetic
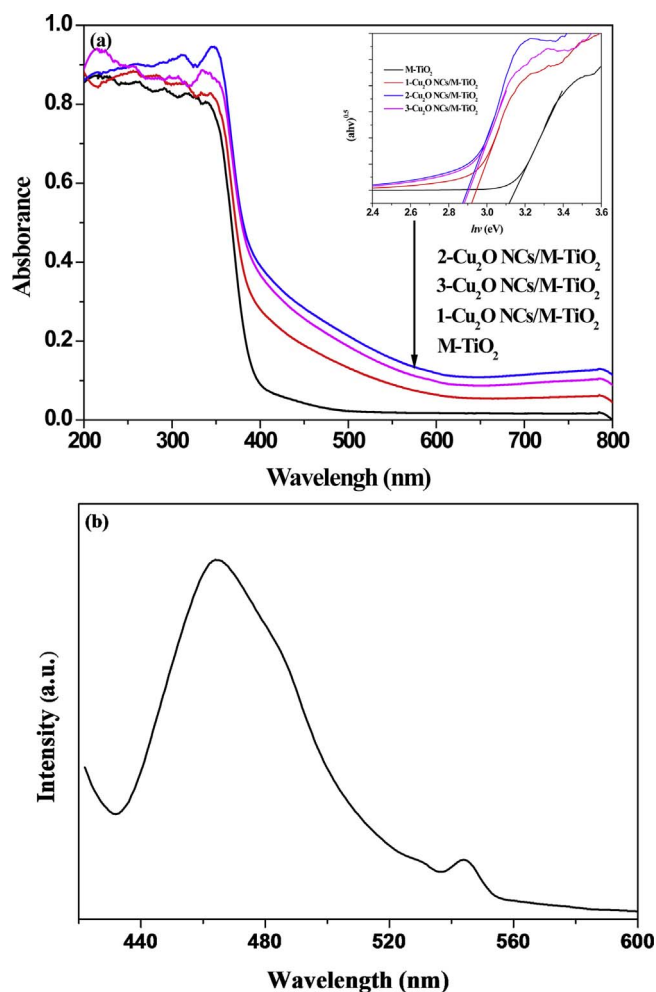
Fig. 3. UV–vis DRS of M-TiO$_2$, 1-Cu$_2$O NCs/M-TiO$_2$, 2-Cu$_2$O NCs/M-TiO$_2$, 3-Cu$_2$O NCs/M-TiO$_2$ (a) and PL spectrum of long-afterglow phosphor (b). Inset is the corresponding Tauc plots for the bandgap estimation of prepared samples.
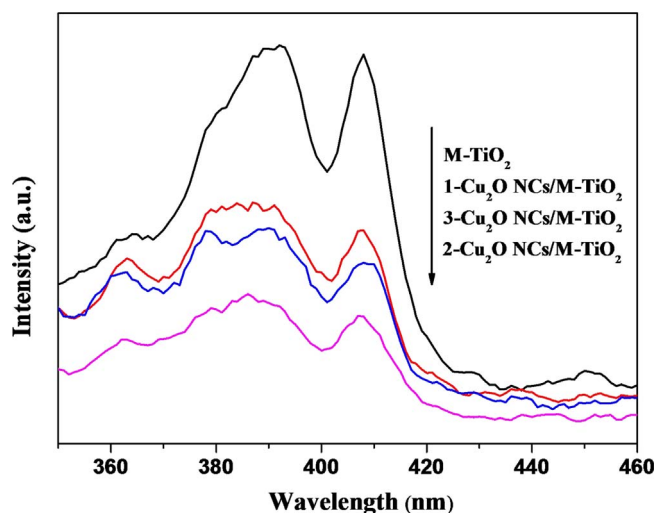
Fig. 4. Photoluminescence spectra measured at room temperature for M-TiO$_2$, 1-Cu$_2$O NCs/M-TiO$_2$, 2-Cu$_2$O NCs/M-TiO$_2$, and 3-Cu$_2$O NCs/M-TiO$_2$. The excitation wavelength was 320 nm.

Fig. 5. Photocurrent measurements (a) and EIS Nyquist plots (b) of prepared phptocatalysts under visible light irradiation.

Fig. 6. The effect of changing rotating speed on the degradation of RhB.

constant (k) and regression coefficients (R^2) were calculated and given in Table S1. The RhB direct photocatalysis and adsorption on catalyst were ignored. Under visible light irradiation, Cu$_2$O NCs displayed the lowest photocatalytic activity owing to its inefficient quantum yield;
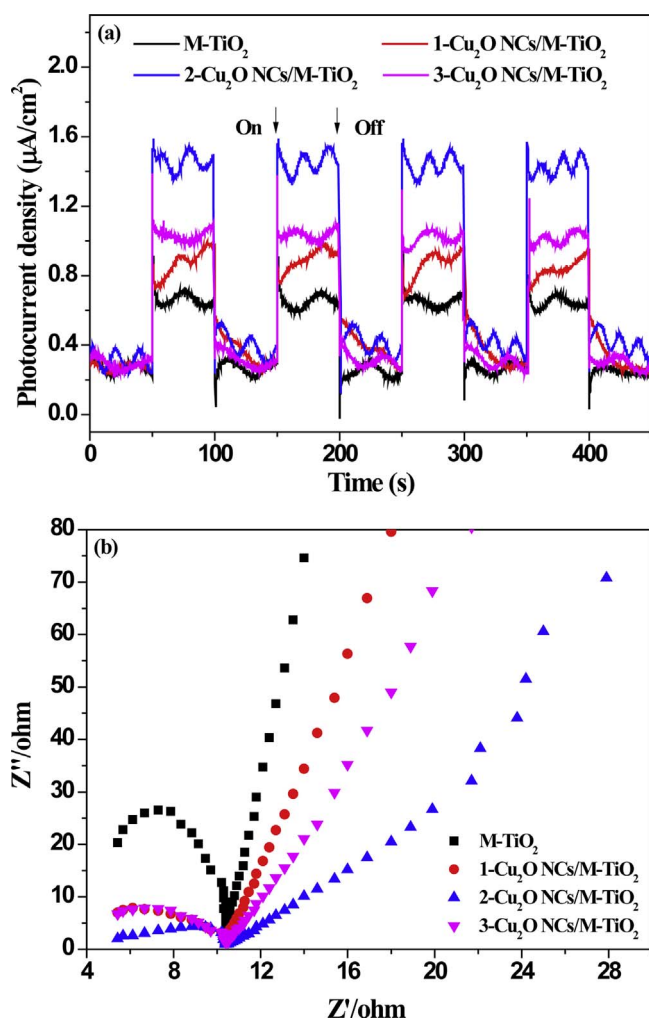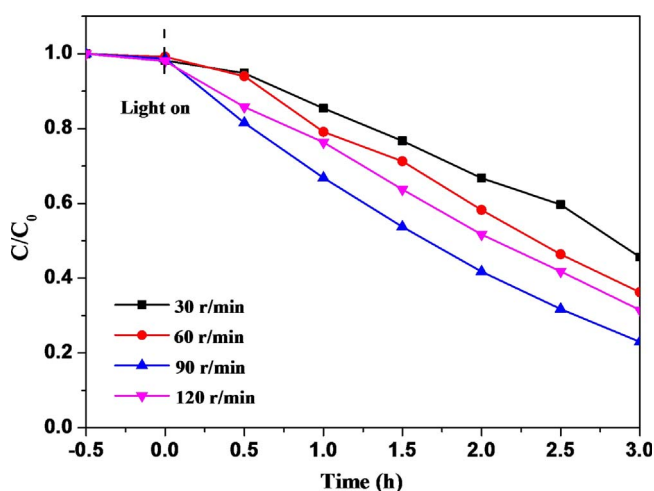
the photocatalytic performance of P25 was also poor because of its narrow optical response range. The contaminate degradation rate of M-TiO$_2$ elevated due to its core-shell microspheres structure which reinforced the interaction between photons and catalyst. The integration of Cu$_2$O NCs raised the photocatalytic reactivity of P25, as shown by the kinetic of 2-Cu$_2$O NCs/P25, which resulted from the improved light
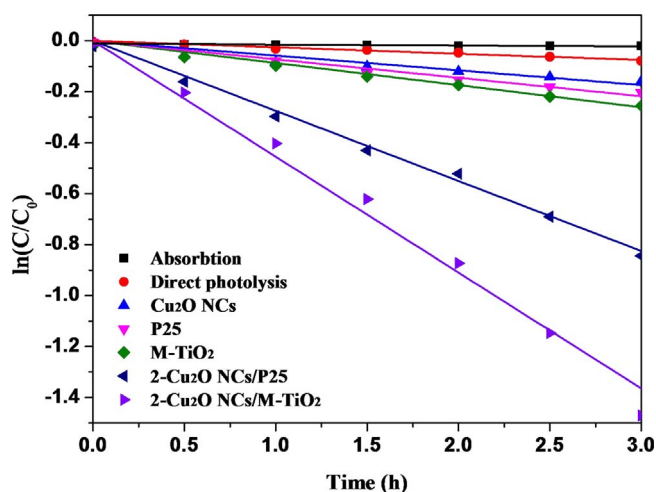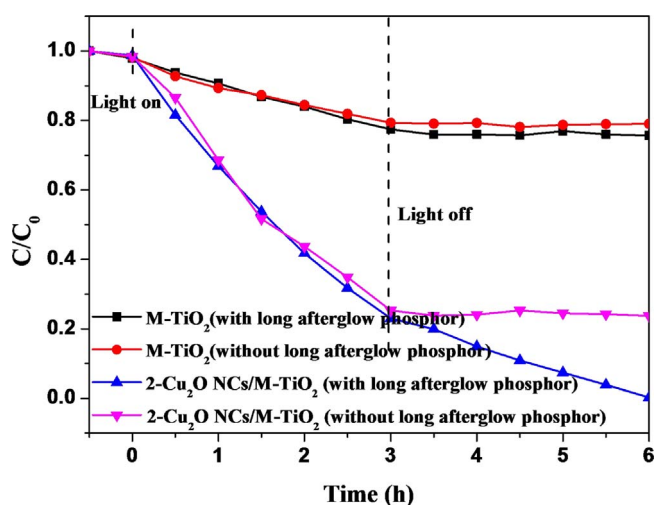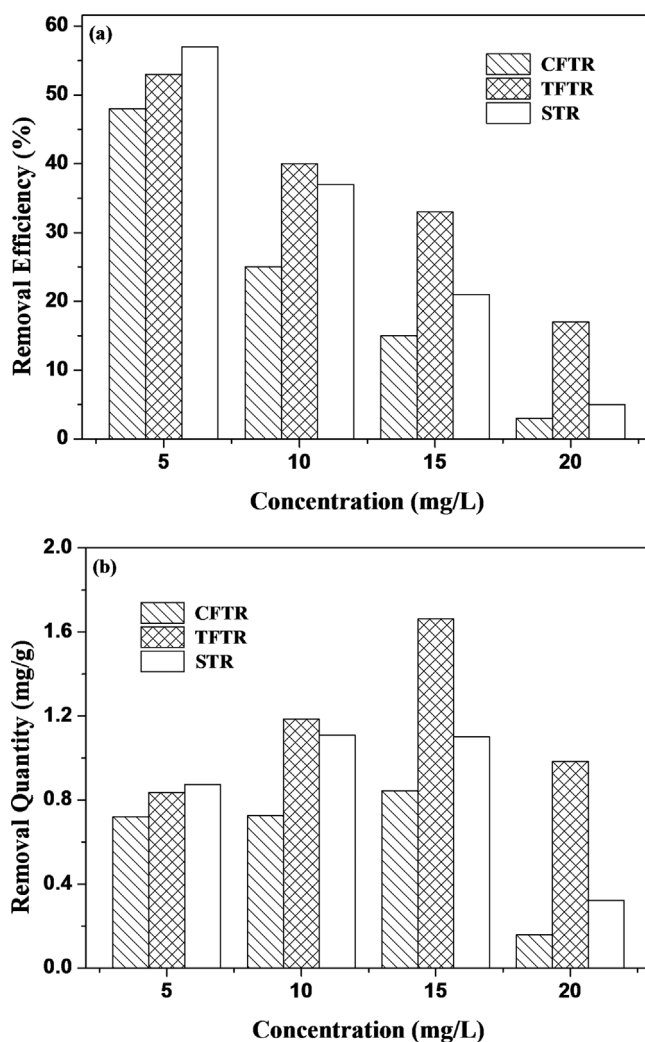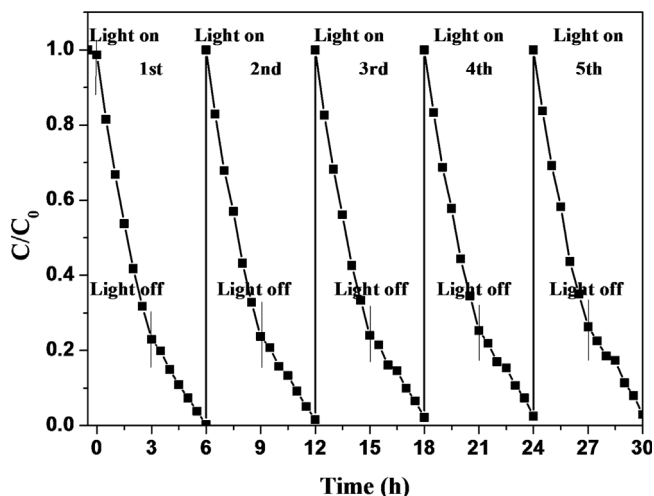
Fig. 7. The kinetics of RhB degradation using various photocatalyst.

Fig. 8. Photodegradation of RhB using M-TiO$_2$ and 2-Cu$_2$O NCs/M-TiO$_2$ in the rotating disk reactor filled with or without long-afterglow phosphor.

Fig. 9. Photodegradation efficiency (a) and removal quantity (b) of RhB using 2-Cu$_2$O NCs/M-TiO$_2$ in TFTR, CFTR, and STR, respectively.

harvesting due to the visible light activity of Cu$_2$O NCs. Among the prepared photocatalysts, 2-Cu$_2$O NCs/M-TiO$_2$ displayed the highest photocatalytic capability, whose kinetic constant was 5.23-fold higher than that using pristine M-TiO$_2$, 7.84-fold larger than that using Cu$_2$O NCs. This improvement benefited from the incorporation of Cu$_2$O NCs which expanded the optical response region of catalyst, and the core-shell structure of M-TiO$_2$ which strengthened the interaction between photons and catalyst by the multiple reflections and scattering of light within microspheres. Additionally, the inner electric field induced by the *p-n* junctions between TiO$_2$ and Cu$_2$O suppressed the recombination of electron/hole pair, finally increasing the quantum yield and the subsequent pollutant degradation efficiency.

3.6.5. Effect of long-afterglow phosphor

Fig. 8 shows the photocatalytic activity of M-TiO$_2$ and 2-Cu$_2$O NCs/M-TiO$_2$ deposited on rotating disk filled with or without long-afterglow phosphor. The photodegradation process consisted of two parts: light on and light off. Under visible light irradiation, the catalysts (M-TiO$_2$ and 2-Cu$_2$O NCs/M-TiO$_2$) in the existence of long-afterglow phosphor presented similar activity to that without long-afterglow phosphor, proving this energy storage material had no effect on the photocatalytic capability of catalysts. When the lamp was switched off, the photocatalytic activity of M-TiO$_2$ almost disappeared, which accounted for the fact that TiO$_2$ cannot be activated by the long-afterglow phosphor

Fig. 10. Recycling test of 2-Cu$_2$O NCs/M-TiO$_2$ film in the rotating-disk reactor filled with long-afterglow phosphor.

whose emission light wavelength was in the range of 430–520 nm, as shown by the PL spectrum in Fig. 3b. However, as expected, the 2-Cu$_2$O NCs/M-TiO$_2$ composites still remained high pollutant decomposition ability even after turning off the light for a long time in the presence of
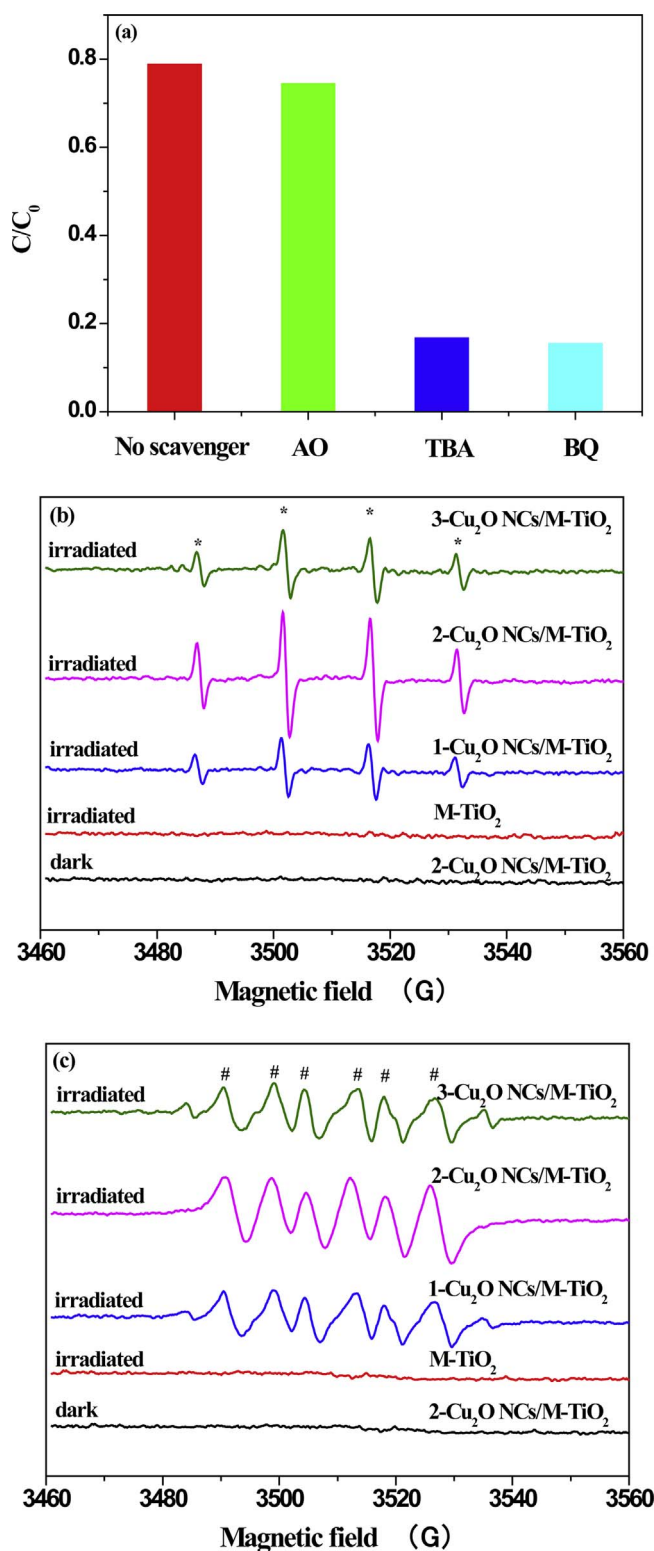
Fig. 11. Trapping experiments of active species (a), DMPO spin-trapping ESR spectra for DMPO-·OH (b), and DMPO-·O_2^- (c). Peaks generated from the DMPO-·OH and DMPO-·O_2^- adducts are marked as (*) and (#), respectively.

long-afterglow phosphor. Similar degradation rates have also been observed in the photocatalytic reaction excited by $Sr_2MgSi_2O_7$: (Eu, Dy) and Blue NL-PA long-afterglow phosphor [8,21]. This result indicated that the long-afterglow phosphor can reserve light energy and give out persistent fluorescence afterward as light source for the RhB decomposition reaction using 2-Cu_2O NCs/M-TiO₂.

3.6.6. Effect of reactor type

Three kinds of photocatalytic systems were designed: (1) thin-film type reactor (TFTR): in which only the upper half of rotating disk was exposed to visible light irradiation, whereas the lower half immersed in pollutants solution was blocked; (2) conventional fixed type reactor (CFTR): where the disk upper part was blocked and the lower part was irradiated by visible light; (3) suspension type reactor (STR): in which Cu_2O NCs/M-TiO₂ with half amount of that deposited on rotating disk was suspended in contaminates solution under magnetic stirring condition. The RhB degradation efficiency in CFTR and STR were used to compare with that in proposed TFTR.

From Fig. 9a, it can be seen that, in the investigated concentration range from 5 to 20 mg/L, the RhB degradation efficiencies in TFTR were much high than those in CFTR, and the decomposition yield difference became broadened as the contaminate concentration increase. The effective RhB degradation in TFTR was mainly attributed to its advantages, in which the photon loss was significantly diminished or even negligible thanks to the shortened optical propagation pathway within thin aqueous film, resulting in improved light utilization yield of photocatalytic system, whereas the photons in CFTR were absorbed by the bulk phase of RhB solution, especially for which with high concentration and heavy colorization. Generally, powder suspension catalysis exhibits better photocatalytic performance than the fixed catalysis owning to its large ratio surface area and effective mass transfer. However, the RhB removal efficiency in STR system was higher than that in TFTR system only when the pollutant concentration was 5 mg/L. As the RhB concentration continually increased, 2-Cu_2O NCs/M-TiO₂ in TFTR displayed better photocatalysis than that in STR. This result indicated the importance of shielding effect elimination to photocatalytic capability improvement. Moreover, compared with STR, there is no problem of recycling difficulty and catalyst loss in this thin film rotating disk reactor.

The absolute RhB removal quantity by per unit mass photocatalyst in TFTR, CFTR, and STR were calculated and presented in Fig. 9b. With the concentration increasing from 5 to 20 mg/L, the actual RhB removal amount first increased and then decreased. The maximum RhB removal quantity achieved when its starting concentration was 15 mg/L, indicating the full treatment capacity of 2-Cu_2O NCs/M-TiO₂ catalyst was reached. The maximum RhB removal amount by per unit mass catalyst in TFTR was 1.97 times as great as that in CFTR, 1.50 times as large as that in STR, suggesting the significance of unique reactor design to photocatalysis enhancement. From the data, we could conclude that in our proposed rotating disk reactor the main pollutant degradation process occurred on the upper half of catalyst disk in TFTR form, whose effectiveness directly determined the total decomposition yield.

3.7. Photocatalytic degradation of BPA

The kinetics of colorless BPA degradation was involved; the corresponding kinetic constants and regression coefficient were displayed in Table S2. From Fig. S6, 2-Cu_2O NCs/M-TiO₂ deposited on rotating disk exhibited much more enhancement in photocatalytic activity than other catalyst, whose kinetic constant was 2.89-fold higher than that using pristine M-TiO₂, 3.84-fold larger than that using Cu_2O NCs. The greatly improved photocatalytic capability demonstrated the merit of this Cu_2O NCs/M-TiO₂ rotating disk reactor for high photocatalytic performance. Additionally, the photosensitized effect could be excluded from the degradation of BPA under visible light irradiation.

Fig. S7 presents the photodegradation efficiency (a) and removal quantity (b) of BPA using 2-Cu_2O NCs/M-TiO₂ in TFTR, CFTR, and STR, respectively. The experimental conditions were as same as that in Fig. 9. It was found that the BPA degradation yields in TFTR were higher than those in CFTR throughout the investigated concentration range. The photocatalytic activity of TFTR was lower than that of STR when the BPA concentration was low, whereas it surpassed that of STR as the BPA concentration exceeded 10 mg/L. When the BPA starting
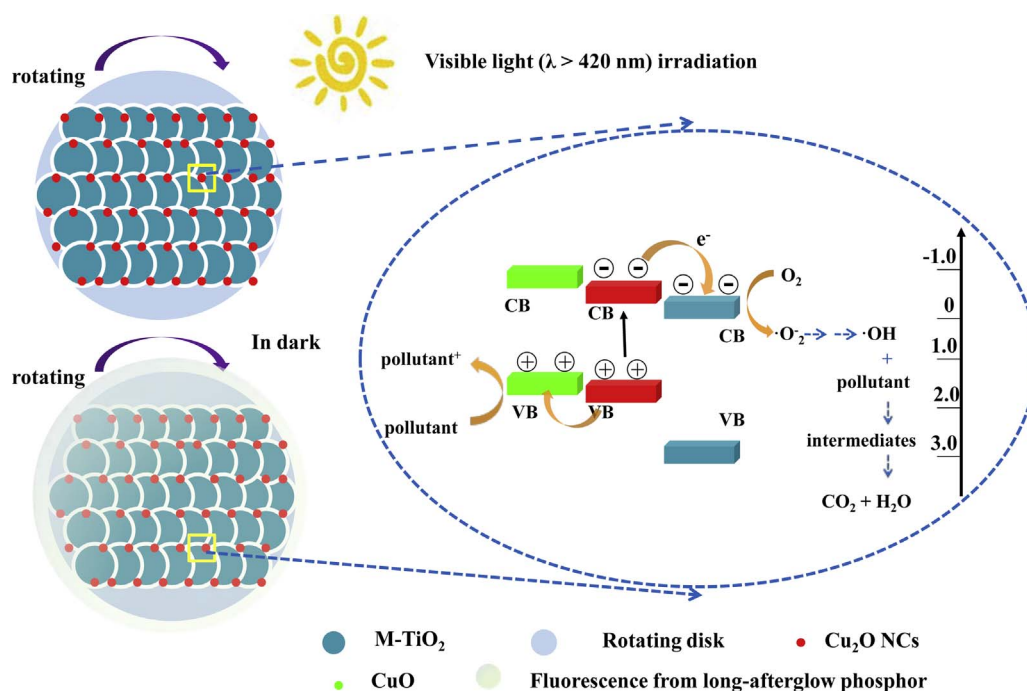
concentration was 15 mg/L, the maximum BPA removal amount achieved, which was 1.27 times as great as that in CFTR, and 1.10 times as large as that in STR. The improvement was lower than that towards RhB degradation, which was ascribed to the weaker light shielding effect and thus the influence of BPA concentration on photocatalytic activity was relatively less.

3.8. Stability of rotating disk reactor assisted by long-afterglow phosphor

Stability of this 2-Cu_2O NCs/M-TiO_2 rotating disk reactor assisted by long-afterglow phosphor was investigated for is importance in practical application. As shown in Fig. 10, there is no significant decrease of photocatalytic ability after five runs and the sample still possessed persistent photocatalytic behavior in darkness, indicating the excellent reliability of this system for enhanced round-the-clock photocatalysis. To investigate the stability of photocatalysts, the SEM images and XPS analyses of repeatedly used sample were characterized. From Fig. S8, the morphology of used 2-Cu_2O NCs/M-TiO_2 did not change remarkably; nanocrystals with the size of 10–20 nm were connected to each other and eventually formed the TiO_2 microspheres in 1.5–4 μm diameter. From Fig. S9, the characteristic peaks of Ti and O did not change significantly compared with those before photocatalytic reactions. As for element copper, the main peaks at 931.9, 947.8, 952.5 and 955.1 eV were witnessed for the band energies of Cu^+ [31,38,47]. While the peaks at 934.5, 938.4 and 942.4 eV were identified to CuO, indicating that Cu_2O was oxidized to CuO during photocatalytic process [48,49]. This CuO could protect Cu_2O from further oxidation by efficiently transferring holes from the valence band of Cu_2O to that of CuO, avoiding the holes accumulation and thus regenerating the catalysts [37,50]. Thus, the instant scavenging of photoinduced carriers ensured the high photocatalytic performance of Cu_2O NCs/M-TiO_2 composite, maintaining good level of reliability. Therefore, we could infer the thin film rotating disk reactor assisted by long-afterglow phosphor should exhibit greater potentials in environmental applications owing to its good photocatalytic reactivity and high reliability.

3.9. Possible reaction mechanism

To reveal the roles of active species involved in Cu_2O NCs/M-TiO_2

photocatalysis, trapping experiments were implemented using tert-butyl alcohol (TBA) as hydroxyl radicals (·OH) scavenger, ammonium oxalate (AO) as holes quencher, and benzoquinone (BQ) as scavenger for superoxide radicals (·O_2^-). As shown in Fig. 11a, when 1 mM AO was added into the photocatalytic system, the pollutant degradation efficiency did not change obviously, which implied the minor role of holes either acting as the oxidizing agent or the origination of ·OH. However, the addition of TBA resulted in a significant decrease in decomposition rate compared to that without any scavenger. Similar retarded pollutant degradation rate was observed in the presence of BQ. Considering above experimental results, it can be deduced that ·OH, originated from the electroreduction of dissolved oxygen with photogenerated electrons via chain reactions, was the vital species in Cu_2O NCs/M-TiO_2 photocatalytic reaction. In order to verify the generation of ·OH and ·O_2^-, the ESR technique was performed. From Fig. 11b and c, it can be seen that almost no signals were detected using M-TiO_2 under visible light irradiation, while obviously characteristic peaks of DMPO-·OH and DMPO-·O_2^- were observed in the Cu_2O NCs/M-TiO_2 photocatalysis. Among these composite catalysts, 2-Cu_2O NCs/M-TiO_2 presented the strongest signals, which was consisted with the photocatalytic performance.

Based on above experimental evidences and instrumental analysis, a possible mechanism of enhanced round-the-clock photocatalysis in this Cu_2O NCs/M-TiO_2 rotating disk reactor assisted by long-afterglow phosphor was put forward and presented in Fig. 12. By rotating the catalyst disk, the light energy loss through absorption by contaminants solution dramatically reduced, increasing the light utilization yield of photocatalytic system, meanwhile the mass transfer on photocatalyst and dissolved oxygen content in solution were enhanced. Under visible light (λ > 420 nm) irradiation, the Cu_2O was excited and generated photocarriers. Because the conduction band of Cu_2O was more negative than that of TiO_2, the electrons could migrate from Cu_2O to TiO_2, reducing the possibility of photoinduced electron/hole pairs recombination [31]. These surviving electrons reduced dissolved oxygen, producing ·O_2^- and the following ·OH which was the dominating active species for pollutant attacking. On the other hand, the holes on Cu_2O could capture electrons from contaminates and thus regenerate catalysts. However, CuO was detected from the XPS spectra of Cu_2O NCs/M-TiO_2 after several photocatalysis, which suggested that the Cu_2O was

self-optimized during the photocatalytic process through a photo-assisted redox reaction. The lower valence band of CuO was in favor of efficient holes transfer from Cu_2O to that, maintaining the high photocatalytic activity and good reliability level of Cu_2O NCs/M-TiO$_2$ composite [37–50]. While under dark condition, the long-afterglow phosphor gave out persistent fluorescence as light source, exciting the Cu_2O NCs/M-TiO$_2$ composite and then achieving enhanced round-the-clock photocatalysis.

4. Conclusions

Overall, a Cu_2O NCs/M-TiO$_2$ rotating disk reactor assisted by long-afterglow phosphor was fabricated for enhanced round-the-clock photocatalysis. By incorporating Cu_2O nanocrystals into TiO$_2$ microspheres, the composite exhibited enlarged optical response region and improved quantum efficiency. Additionally, the light utilization yield of photocatalytic system was improved through avoiding the light shielding effect by solution via keeping the catalyst disk rotation. Finally, with the assistance of long afterglow phosphor, the round-the-clock photocatalysis was achieved, indicating the development of a full-time active highly efficient photocatalysts system. We believe this work could provide an important and selfcontained methodology for developing round-the-clock photocatalysts, pushing the full industrialization of photocatalytic technology.

Acknowledgments

Appendix A. Supplementary data

Supplementary data associated with this article can be found, in the online version, at http://dx.doi.org/10.1016/j.apcatb.2017.10.054.

References

[1] P.A. Pekakis, N.P. Xekoukoulotakis, D. Mantzavinos, Water Res. 40 (2006) 1276–1286.
[2] N.N. Rao, V. Chaturvedi, G.L. Puma, Chem. Eng. J. 184 (2012) 90–97.
[3] R. Yuan, R. Guan, P. Liu, J. Zheng, Colloids Surf, A Physicochem. Eng. Aspects 293 (2007) 80–86.
[4] M.Y. Ghaly, T.S. Jamil, I.E. El-Seesy, E.R. Souaya, R.A. Nasr, Chem. Eng. J. 168 (2011) 446–454.
[5] J. Saien, H. Nejati, J. Hazard. Mater. 148 (2007) 491–495.
[6] M.N. Chong, B. Jin, J. Hazard. Mater. 199–200 (2012) 135–142.
[7] H.H. Li, S. Yin, Y.H. Wang, T. Sato, J. Catal. 286 (2012) 273–278.
[8] Q. Zhou, F.P. Peng, Y.R. Ni, J.H. Kou, C.H. Lu, Z.Z. Xu, J. Photochem. Photobiol. A 328 (2016) 182–188.
[9] Y.N. Huo, X.F. Chen, J. Zhang, G.F. Pan, J.P. Jia, H.X. Li, Appl. Catal. B 148–149 (2014) 550–556.
[10] Y.N. Huo, R.J. Hou, X.F. Chen, H.B. Yin, Y. Gao, H.X. Li, J. Mater. Chem. A 3 (2015) 14801–14808.
[11] K. Li, H.B. Zhang, Y. He, T.T. Tang, D.W. Ying, Y.L. Wang, T.H. Sun, J.P. Jia, Chem. Eng. J. 268 (2015) 10–20.
[12] Z. Yu, F. Li, L.C. Sun, Energy Environ. Sci. 8 (2015) 760–775.
[13] M. Liu, K. Sunada, K. Hashimoto, M. Miyauchi, J. Mater. Chem. A 3 (2015) 17312–17319.
[14] Y.H. Lin, Z.L. Tang, Z.T. Zhang, X.L. Wan, J.Y. Zhang, J. Mater. Sci. Lett. 20 (2001) 1505–1506.
[15] H.H. Li, S. Yin, T. Sato, Appl. Catal. B 106 (2011) 586–591.
[16] H.H. Li, S. Yin, Y.H. Wang, T. Sato, Environ. Sci. Technol. 46 (2012) 7741–7745.
[17] H.H. Li, S. Yin, Y.H. Wang, T. Sekino, S.W. Lee, T. Sato, J. Mater. Chem. A 1 (2013) 1123–1126.
[18] J.A. Zeevalkink, P. Kelderman, C. Bouelhouwer, Water Res. 12 (1978) 577–581.
[19] G. Dionysiou, M.T. Balasubramanian, A.P. Suidan, I. Baudin, J.M. Laîné, Water Res. 34 (2000) 2927–2940.
[20] D.D. Dionysiou, A.P. Khodadoust, A.M. Kern, M.T. Suidan, I. Baudin, J.M. Laîné, Appl. Catal. B 24 (2000) 139–155.
[21] Y.B. Yin, X.F. Chen, R.J. Hou, H.J. Zhu, S.Q. Li, Y.N. Huo, H.X. Li, ACS Appl. Mater. Interfaces 7 (2015) 20076–20082.
[22] J. Choi, H. Park, M.R. Hoffmann, J. Phys. Chem. C 114 (2010) 783–792.
[23] I. Krivtsov, M. Ilkaeva, E. Salas-Colera, Z. Amghouz, J.R. García, E. Díaz, S. Ordóñez, S. Villar-Rodil, J. Phys. Chem. C 121 (2017) 6770–6780.
[24] P. Chowdhury, J. Moreira, H. Gomaa, A.K. Ray, Ind. Eng. Chem. Res. 51 (2012) 4523–4532.
[25] W.D. Kim, J.H. Kim, S. Lee, S. Lee, J.Y. Woo, K. Lee, W.S. Chae, S. Jeong, W.K. Bae, J.A. McGuire, J.H. Moon, M.S. Jeong, D.C. Lee, Chem. Mater. 28 (2016) 962–968.
[26] T.X. Liu, X.Z. Li, F.B. Li, Environ. Sci. Technol. 42 (2008) 4540–4545.
[27] Y. Lu, H.T. Yu, S. Chen, X. Quan, H.M. Zhao, Environ. Sci. Technol. 46 (2012) 1724–1730.
[28] L.X. Yang, W.S. Sun, S.L. Luo, Y. Luo, Appl. Catal. B 156–157 (2014) 25–34.
[29] J.S. Luo, L. Steier, M.K. Son, M. Schreier, M.T. Mayer, M. Grätzel, Nano Lett. 16 (2016) 1848–1857.
[30] J.F. Zhang, Y. Wang, C.P. Yu, X. Shu, L. Jiang, J.W. Cui, Z. Chen, T. Xie, Y.C. Wu, New J. Chem. 38 (2014) 4975–4984.
[31] Z. Geng, Y. Zhang, X. Yuan, M.X. Huo, Y.H. Zhao, Y. Lu, Y. Qiu, J. Alloy. Compd. 644 (2015) 734–741.
[32] M.E. Aguirre, R.X. Zhou, A.J. Eugene, M.I. Guzman, M.A. Grela, Appl. Catal. B 217 (2017) 485–493.
[33] C.W. Guo, Y. Cao, S.H. Xie, W.L. Dai, K.N. Fan, Chem. Commun. (2003) 700–701.
[34] G.Z. Liao, S. Chen, X. Quan, Y.B. Zhang, H.M. Zhao, Appl. Catal. B 102 (2011) 126–131.
[35] J. Hensel, G. Wang, Y. Li, J.Z. Zhang, Nano Lett. 10 (2010) 478–483.
[36] S.M. Park, A. Razzaq, Y.H. Park, S. Sorcar, Y. Park, C.A. Grimes, ACS Omega 1 (2016) 868–875.
[37] X. Xu, Z.H. Gao, Z.D. Cui, Y.Q. Liang, Z.Y. Li, S.L. Zhu, X.J. Yang, J.M. Ma, ACS Appl. Mater. Interfaces 8 (2016) 91–101.
[38] Z.Y. Zhang, K.C. Liu, Y.N. Bao, B. Dong, Appl. Catal. B 203 (2017) 599–606.
[39] Y. Cong, X. Li, Y. Qin, Z. Dong, G. Yuan, Z. Cui, X. Lai, Appl. Catal. B 107 (2011) 128–134.
[40] S.S. Zhang, S.Q. Zhang, F. Peng, H.M. Zhang, H.W. Liu, H.J. Zhao, Electrochem. Commun. 13 (2011) 861–864.
[41] J.H. Yang, J. Wang, X.Y. Li, D.D. Wang, H. Song, Catal. Sci. Technol. 6 (2016) 4525–4534.
[42] P.F. Wang, S.H. Zhan, Y.G. Xia, S.L. Ma, Q.X. Zhou, Y. Li, Appl. Catal. B 207 (2017) 335–346.
[43] C.H. Zhang, L.H. Ai, J. Jiang, Ind. Eng. Chem. Res. 54 (2015) 153–163.
[44] Y.P. Zhu, T.Z. Ren, Z.Y. Yuan, ACS Appl. Mater. Interfaces 7 (2015) 16850–16856.
[45] Y.L. Xu, Y. He, X.D. Cao, D.J. Zhong, J.P. Jia, Environ. Sci. Technol. 43 (2008) 2612–2617.
[46] K. Li, C. Yang, Y.L. Xu, D.W. Ying, Y.L. Wang, J.P. Jia, Chem. Eng J. 211–212 (2012) 208–215.
[47] R.A. Rather, S. Singh, B. Pal, J. Catal. 346 (2017) 1–9.
[48] L.M. Liu, W.Y. Yang, Q. Li, S.A. Gao, J.K. Shang, ACS Appl. Mater. Interfaces 6 (2014) 5629–5639.
[49] H.Y. Zhang, P.P. Dong, Y.H. Ni, J. Gao, Mater. Charact. (2017), http://dx.doi.org/10.1016/j.matchar.2017.09.011.
[50] Y. Xu, M.A. Schoonen, Am. Mineral. 85 (2000) 543–556.